ACCSCIENCE PUBLISHING

Materials Science in Additive Manufacturing

ORIGINAL RESEARCH ARTICLE

Topology optimization of an aluminum bicycle pedal crank using laser powder bed fusion

Jose Manuel Costa[1,2]*, Mariana Cerqueira Maia[1], Adriana Pinho Fernandes[1], Elsa Costa Oliveira[1], Manuel Fernando Vieira[1,2], and Elsa Wellenkamp Sequeiros[1,2]

[1]Department of Mechanical Engineering, Faculty of Engineering, University of Porto, Porto, Portugal

[2]LAETA, Institute of Science and Innovation in Mechanical and Industrial Engineering, Porto, Portugal

Abstract

This study investigates the application of topology optimization (TO) in combination with laser powder bed fusion (LPBF) to design a lightweight, high-performance bicycle pedal crank using AlSi10Mg alloy. The optimization process was carried out using Fusion 360 and nTopology, resulting in a 20% mass reduction while ensuring compliance with the ISO 14781 standards for pedal cranks. The component was characterized in terms of microstructure, surface roughness, dimensional accuracy, powder distribution, and Vickers hardness. The microstructure exhibited the characteristic melt pool patterns associated with LPBF, indicative of the manufacturing process. Surface roughness measurements showed a mean value of 23.4 µm, with dimensional analysis revealing a mean deviation of 7% from nominal dimensions. The powder distribution analysis indicated a narrow particle size distribution, contributing to consistent print quality. The component's hardness was measured at 134 HV0.3, highlighting its promising mechanical properties. This work demonstrates the potential of TO and LPBF to produce structurally optimized, lightweight components with enhanced performance, providing valuable insights into the application of Design for Additive Manufacturing for metallic materials.

Keywords: Bike crank; AlSi10Mg; Laser powder bed fusion; Design for Additive Manufacturing; Topology optimization; Metallographic characterization; Roughness dimensional analysis; Powder characterization

***Corresponding author:**
Jose Manuel Costa
(jose.costa@fe.up.pt)

Citation: Costa JM, Maia MC, Fernandes AP, Oliveira EC, Vieira MF, Sequeiros EW. Topology optimization of an aluminum bicycle pedal crank using laser powder bed fusion. *Mater Sci Add Manuf.* 2025;4(1):025040003. doi: 10.36922/MSAM025040003

Received: January 24, 2025

1st revised: February 15, 2025

2nd revised: February 18, 2025

3rd revised: February 20, 2025

Accepted: February 21, 2025

Published online: March 26, 2025

1. Introduction

Technological advancements continue to revolutionize the manufacturing sector, with additive manufacturing (AM) at the forefront of these innovations. AM is poised to significantly impact sustainability and society at large, offering transformative solutions across various industries.[1] ISO/ASTM 52900:2021 defines AM as joining materials to fabricate parts from three-dimensional (3D) model data, typically layer upon layer, diverging from traditional subtractive and formative manufacturing methodologies.[2,3] This method facilitates the construction of lightweight structures with complex geometries by emulating biological processes inspired by biomimetic principles.[4] The principal advantages of AM include diminished production expenses, enhanced

geometric versatility, customization potential, generative design, and waste minimization.[5,6] These attributes are pivotal across environmental, social, and economic dimensions.[3,7]

Even with this, AM has limitations. It has not fulfilled all prognosticated expectations despite being integrated into the big data revolution. Compared to traditional manufacturing techniques, challenges include mass production scalability, size constraints, surface finishing imperfections, and the costs associated with raw materials, equipment, and initial capital.[8,9]

Various AM technologies have been broadly adopted, including fused filament fabrication, powder bed fusion (PBF), stereolithography, selective laser sintering, and digital light processing.[10,11] The selection among these technologies is predicated on the desired functional, esthetic, and mechanical outcomes alongside financial considerations.[12] Critical factors include part volume, layer volume, material deposition rate, and the balance between material flexibility and mechanical requirements. AM materials span polymers, metals, ceramics, and composites in diverse forms such as liquid, wire, powder, or sheet.[9,12,13]

AM furnishes extensive modeling capabilities through various design instruments that enable engineers and designers to forecast mechanical responses and economic viability and automate part manufacturing processes.[14] Among these, PBF systems, capable of utilizing either electron beam or laser energy sources, offer exceptional versatility. This article focuses on laser PBF (LPBF), an AM technology classified by ISO/ASTM. LPBF employs concentrated thermal energy from a laser to fuse materials, depositing them layer by layer.[10]

The LPBF process is initiated with a 3D computer-aided design (CAD) model and machine programming, encompassing material loading, thermal heating, and environmental setup (either vacuum or protective gas). A recoater deposits a powder layer onto a construction plate, followed by selective laser melting of the powder according to predetermined parameters. The construction plate descends for each layer, replicating the process until the component is complete. Post-processing involves component removal, heat treatment, and finishing to achieve desired performance standards.[1]

Raw material characteristics are vital in the LPBF process, determining the final component's mechanical and physical properties. Spherical powders, produced through gas atomization, are preferred for their enhanced fluidity during deposition, contributing to reduced porosity and satisfactory surface quality.[15,16] The spherical geometry aids in stable molten pool formation and elevated packing density – Van der Waals forces, particle radius, and friction influence powder flowability. Smaller particles with increased surface areas encounter augmented Van der Waals forces and friction, impeding fluidity during layer formation. Non-spherical shapes further augment the surface area, adversely affecting flowability.[17-21]

AM technologies, such as LPBF, provide the flexibility to fabricate complex geometries and intricate internal features. By integrating Design for AM (DfAM), the design process can be optimized to leverage these capabilities fully, enabling the production of lightweight, highly functional parts.[22-24] Topology optimization (TO) is used in the DfAM approach, and it is a numerical approach that identifies the optimal material distribution within a given design space to achieve the desired functionality, enhancing performance while minimizing material usage.[25-27] The TO approach algorithmically determines the most structurally efficient design within a defined space and under given constraints, resulting in organic, optimized shapes that use material only where necessary for structural integrity.[23,28,29]

The integration of TO (and DfAM) in AM enhances components' structural performance and material efficiency and plays a significant role in improving the sustainability of manufacturing processes. TO reduces material waste, optimizes distribution within a given design space, and ensures that only the necessary material is used for structural integrity. This reduces both the material consumption and the overall weight of the part, contributing directly to sustainability. TO and AM technologies such as LPBF contribute to energy efficiency.[30,31] The ability to fabricate complex geometries that would be impossible or highly inefficient to produce using traditional subtractive manufacturing methods allows for more efficient use of resources. By reducing material usage and minimizing waste during the manufacturing process, TO and AM provide an effective strategy for lowering the environmental impact of industrial production.[3,23]

Previous studies, such as those by Mata *et al.*[32] and Oliveira *et al.*,[24] have explored the successful integration of DfAM and TO in designing various components, showcasing how these approaches enable the creation of highly efficient, lightweight structures. Mata *et al.* optimized a metal door-handle design using nTopology and AM, focusing on lattice structures and generative design to reduce weight and enhance mechanical properties. Similarly, Oliveira *et al.* applied DfAM and TO to an office stapler, leveraging MEX technology for mass reduction without compromising the part's mechanical integrity. These studies illustrate the effectiveness of DfAM and TO in producing lightweight, efficient structures, a

crucial aspect for applications in industries ranging from aerospace to consumer products.

In this context, LPBF is particularly advantageous for materials such as AlSi10Mg, an aluminum alloy known for its low density, high thermal conductivity, and good mechanical properties. This makes AlSi10Mg ideal for creating lightweight, cost-efficient products. The integration of DfAM and TO enhances LPBF by optimizing material distribution within a design space, enabling the creation of complex geometries, including internal lattices, which are often impractical or impossible to achieve with traditional manufacturing methods.[1,33,34]

This investigation endeavors to optimize a bicycle pedal crank component for fabrication through AM, explicitly employing LPBF with an aluminum alloy (AlSi10Mg). The objective is to substantiate its production viability and catalyze interest for future integration into the market.

2. Materials and methods

2.1. TO and manufacturing

The first step in designing the bike component was to model the conventional component. For this, the Shimano SLX M7000 Hollowtech II Crank[35] was used as a base model with a crank length of 170 mm. The conventional model was developed to fit an 82/61 mm pedal. Figure 1 shows the model canvas and the resulting component.

From this point onward, the optimization process for AM began to minimize the mass of the component while ensuring a safety factor of 2 as per the typical design standards. It was essential to define the design variables, which were chosen based on a typical usage scenario for a bicycle pedal crank and the requirements outlined in ISO 14764:2022.[36] According to this standard, the deflection of the crank arm should not exceed 20%. The standard specifies that a fatigue test must be performed to assess the component's performance, with a dynamic force of 1300 N

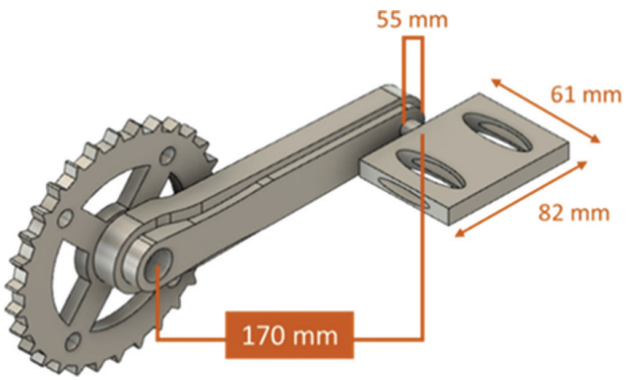

Figure 1. Model canvas and the resulting modeling component of a conventional bike crank

applied over 100,000 cycles.[36] In this study, however, the safety factor was not directly measured but retrieved from industry standards and bibliographical sources that align with the material properties and typical loading conditions for similar components. This was used as a design criterion to guide the optimization process.

The TO process used the GD module in Autodesk Fusion 360 (San Francisco, CA, USA). The following procedure was adopted to achieve an optimized design suitable for AM:

1. *Initial setup.* The optimization began by defining the geometries to preserve (parts of the component that need to remain intact) and obstacle geometries (areas where material could not be added). These parameters were essential to ensure the final design adhered to functional and manufacturing constraints
2. *Design constraints and load cases.* A set of boundary conditions and load cases was applied, as prescribed by ISO 14781.[10] These constraints included:
   (a) Pin and fixed geometries: To simulate the component's attachment to the bike and fix its orientation
   (b) A 1300 N load was applied to the crank arm, simulating the forces during cycling
   (c) A safety factor of 2 was defined to ensure the design met structural integrity requirements under typical operating conditions
3. *Material selection.* The material selected for the optimization process was AlSi10Mg alloy, chosen for its low density and high specific mechanical resistance (UTS/density, Young's modulus/density), making it ideal for LPBF applications
4. *Manufacturing constraints.* The AM process was defined with specific constraints:
   (a) An overhang angle of 45° was allowed to ensure manufacturability
   (b) A minimum material thickness of 3 mm was enforced to maintain the part's structural integrity during printing
5. *Optimization and design generation.* The optimization process was executed using Fusion 360's GD module, which utilized the specified load cases and constraints to generate the optimized crank model. The resulting design aimed to reduce mass while maintaining the required safety factor and ensuring functionality.

The study setup and the resulting best outcome are shown in Figure 2.

After generating the optimized model, it was subjected to a simulated static test in the software's simulation module. The same constraints and loads used for the optimization were considered. Based on the resulting

values and the designer's critical opinion, some adaptations were made to improve the component to improve the safety factor to 5. When a safety factor of 5.24 was attained, the component was transferred to new software, nTopology. The topologically optimized was used to add interior (Figure 3A) and external lattices (Figure 3B) to the component. The lattices were introduced to increase the complexity of the part in the study since this research has developed as a hands-on teaching technique. The first lattice was created in the solid part of the component, and the exterior lattice was used to substitute the central depression in the model, intending to decrease mass and improve esthetic appeal.

In the TO process, the first step involved the introduction of an internal lattice within the solid part of the component (Figure 3A). This lattice structure was specifically designed to optimize the internal support of the crank while simultaneously reducing the overall mass. Following this, an external lattice structure was applied to replace the central depression in the crank (Figure 3B). The external lattice not only aimed to reduce the weight further but also contributed to the esthetic appeal of the part, ensuring that both functional and visual considerations were addressed in the optimization process.

Once the optimized design with the added lattices was finalized, a final static test was conducted within nTopology, maintaining the same load and displacement constraints. The results of these tests will be discussed in section 3.2.

The LPBF process was used to manufacture the final component. The components were produced using a Renishaw AM400 machine (Wotton-under-Edge, United Kingdom) at Hypermetal–Metal AM (Porto, Portugal). The manufacturing process was prepared using Renishaw's software, which defined the part orientation, added necessary supports, and adjusted the laser parameters for optimal printing.

The part was printed using 30-micron layers with a stripe strategy and block path. To conserve resources, the bike crank was produced at a 1/5th scale. Once printed, the supports were mechanically removed, and the part was micro-sandblasted using a Guyson machine (North Yorkshire, United Kingdom).

Despite the scale reduction, all static simulations were performed with the accurate dimensions of the full-size crank. The size reduction impacts only manufacturability, as it could present challenges in ensuring adequate heat dissipation in intricate features, such as lattices, which could affect print success.

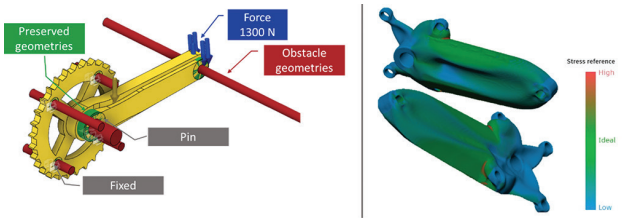

Figure 2. Study setup and the best resulting bike crank (the color scheme displays the stress distribution on the safety factor defined)

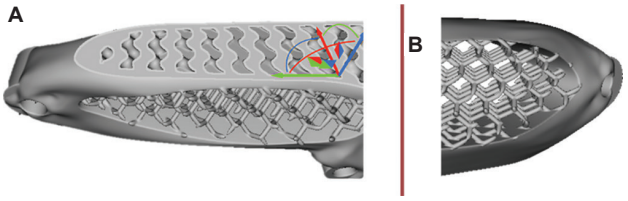

Figure 3. Topology optimization of a bike crank. (A) Interior lattice developed in the solid part of the component; (B) exterior lattice developed in the central depression

2.2. Powder characterization and chemical composition of AlSi10Mg alloy

This study used powders of an aluminum alloy, AlSi10Mg, from Osprey (Sandvik, Sandviken, Sweden). The chemical composition is shown in Table 1.

Figure 4 shows scanning electron microscopy (SEM) images of AlSi10Mg metal powders supplied by Hypermetal (Porto, Portugal), using Osprey powder as the feedstock material. The powders were analyzed using SEM/energy-

Table 1. Chemical composition of AlSi10Mg alloy from Osprey[37]

Al	Si	Mg	Fe	Ti	Mn	Cu	Ni
Balance	9 – 11	0.2 – 0.4	≤0.55	≤0.15	≤0.45	≤0.03	≤0.04

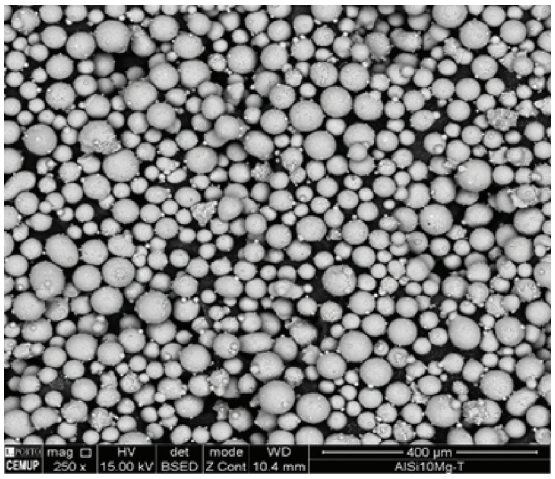

Figure 4. SEM images of AlSi10Mg metal powders supplied
Abbreviation: SEM: Scanning electron microscopy

dispersive X-ray spectroscopy electron microscopy at the Materials Centre of the University of Porto (CEMUP, Porto, Portugal).

The study focused on three zones (indicated in Figure 5), confirming the predominant presence of aluminum, silicon, and magnesium in the matrix, which aligns with the nominal chemical composition of the alloy.

2.3. Metallography and roughness measurement

To avoid the destruction of the topologically optimized component in its mechanical characterization, Hypermetal provided an additional cube with a prismatic shape, produced under the same processing conditions as the topologically optimized bicycle pedal crank using LPBF. The prismatic sample was chosen to facilitate microstructural characterization and surface roughness measurements, which were more easily performed on this simpler geometry than the pedal crank's complex geometry. Due to the pedal crank intricate shape, it was challenging to achieve flat surfaces for accurate roughness testing. A schematic representation of the experimental procedure, including the use of both the prismatic sample and the pedal crank, is shown in Figure 6.

The surface roughness analysis was achieved using the LAX software and was conducted on two components, aiming for a more precise construction of the topological profile, considering different axial references. In parallel, a non-destructive visual inspection test was performed to detect possible surface defects. The cutting was done with an abrasive disc in the equipment designated for this purpose – Presi Mecatome T210 (Eybens, France). The metallographic preparation comprised the steps of hot mounting in acrylic resin, using the equipment Buehler SIMPLIMET 1000 (Leinfelden-Echterdingen, Germany), grinding to 4000 µm abrasive sandpaper, smoothing in 1 µm cloth, and etching (0.5% hydrofluoric acid + 99.5% water) for 1 min. Micrography was obtained using the Leica® DVM6 (Wetzlar, Germany) equipment and its analysis software – LAX. Thus, the melt pool size was not directly measured in this study, it influences heat distribution and solidification is a known factor in LPBF. Understanding its potential impact on material properties is important. While the precise measurement of melt pool size requires further experimentation, this study focused on optimizing process parameters that influence the final part quality. The dimensions of the melt pools were measured using the image processing software ImageJ on the micrographs obtained. Finally, to complete the mechanical characterization, Vickers microhardness measurements were carried out with SHIMADZU M microdurometer (Kyoto, Japan) and Duramin software (Kyoto, Japan) along 14 sample points, applying a weight of 0.3 kgf following standard ISO 6507-1: 2011.

3. Results and discussion

3.1. Microstructure analysis

Figure 7 presents the microstructure of an AlSi10Mg component produced via LPBF, revealing a characteristic fish-scale pattern of molten pools that emphasizes the build direction. The microstructure displays elongated cells along the laser scan path, while cells appear more equiaxed in the direction perpendicular to the scan path. Three distinct regions within the melt pool microstructure are observable: the core of the pool, which contains finer cellular structures; an intermediate region characterized by coarser cells; and the heat-affected zone, which exhibits a partially disrupted cellular structure. The heat-affected zone is typically found at the boundary of the melt pools, where the cooling rates diverge significantly, leading to microstructural variation and changes in material properties such as strength and porosity.[38]

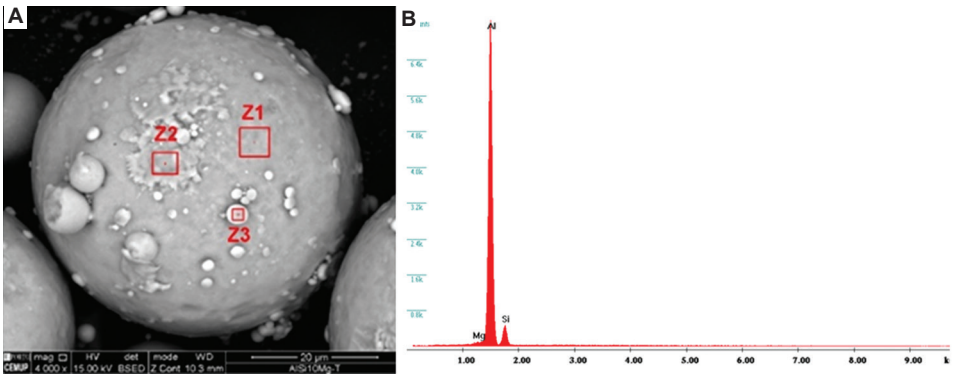

Figure 5. SEM/EDS analysis of AlSi10Mg powders. (A) SEM image shows the locations of the analysis areas marked as Z1, Z2, and Z3, selected for EDS analysis. Scale bar: 20 µm. (B) The corresponding EDS spectrum of the analyzed powder confirms the predominant presence of aluminum (Al), silicon (Si), and magnesium (Mg), consistent with the nominal chemical composition of the alloy
Abbreviation: EDS: Energy dispersive X-ray spectroscopy; SEM: Scanning electron microscopy

While melt pool size was not the primary focus of this study, it is essential for understanding heat distribution and solidification behavior during LPBF. As demonstrated in previous studies,[1,2] melt pool dimensions significantly influence material properties, including porosity, strength, and microstructural integrity. To accurately characterize these effects, it is recommended that future investigations employ single-track experiments, which provide more precise measurements of the melt pool, especially at the top surface (last layer), where no subsequent layers affect the measurements.

1 A novel paradigm for feedback control in LPBF: layer-wise correction for overhang structures
E. Vasileska, A. G. Demir, B. M. Colosimo and B. Previtali
Advances in Manufacturing 2022 Vol. 10 Issue 2 Pages 326-344
DOI: 10.1007/s40436-021-00379-6

2 A Review on Discrete Element Method Simulation in Laser Powder Bed Fusion Additive Manufacturing
H. Chen, Y. Sun, W. Yuan, S. Pang, W. Yan and Y. Shi
Chinese Journal of Mechanical Engineering: Additive Manufacturing Frontiers 2022 Vol. 1 Issue 1 Pages 100017
DOI: https://doi.org/10.1016/j.cjmeam.2022.100017

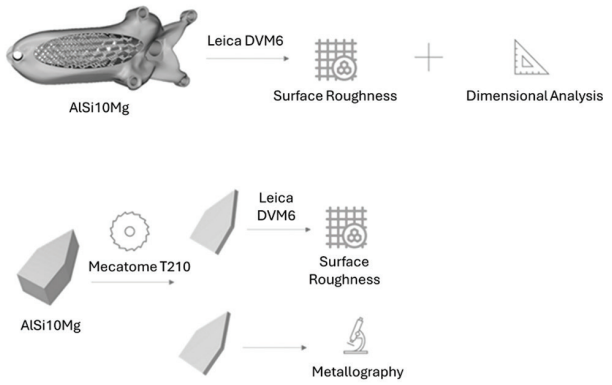

Figure 6. Experimental procedure for microstructural and mechanical characterization

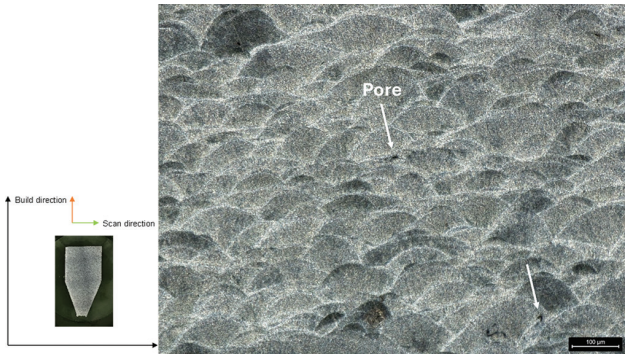

Figure 7. An optical micrograph of melt pools perpendicular to the build direction of AlSi10Mg shows the characteristic fish-scale pattern, with elongated cells along the laser scan path and equiaxed cells perpendicular to it. Scale bar: 100 μm

In this study, melt pool dimensions were analyzed using ImageJ software (Figure 8), revealing an average width (W) of 153.6 μm (in purple) and a depth (h) of 60.7 μm (in green). These values were obtained from the laser scan tracks on the last layer, as these tracks are unaffected by remelting during subsequent layers. For a more detailed characterization of the melt pool, including its chemical composition and morphological changes, we recommend utilizing advanced techniques such as transmission electron microscopy (TEM),[39] and SEM with electron backscatter diffraction.[38,40,41]

3.2. Simulation of static test

The topologically optimized component (Figure 2), with an initial mass of 886 g, underwent a static load test under a 1300 N load. The maximum local stress during static loading under 1300 N is 214 MPa, which is below the yield strength of AlSi10Mg (240 MPa). This results in a safety factor of 1.12. While no plastic deformation is expected under typical loading conditions, elastic deformation may still occur, particularly in the lattice structure. Lattice structures, designed to optimize material usage and reduce weight, behave differently under load than solid components due to internal voids. These internal voids lead to localized strain, resulting in elastic deformation without exceeding the yield strength. This deformation is reversible, and the material returns to its original shape once the load is removed. While the simulation suggests that the component will not undergo permanent deformation under the applied load, the safety factor derived from stress analysis may vary depending on the specific criteria and calculation method. Simulation plays a crucial role in predicting the mechanical behavior of components and guiding design adjustments before manufacturing. However, static simulations are not a substitute for empirical mechanical testing. Fatigue testing remains essential to ensure

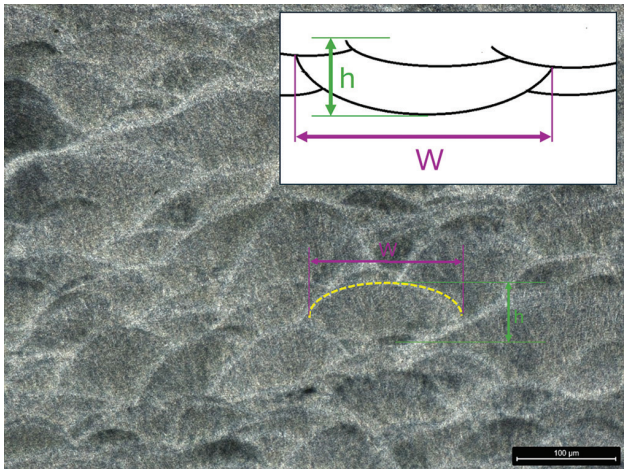

Figure 8. Melt pools' dimensions. Scale bar: 100 μm

compliance with industry standards and verify long-term durability under cyclic loading conditions.

Figure 9A and B present the final component obtained. Strain distribution in the component was relatively uniform, with a maximum value of 0.0016. The maximum stress, an important metric for evaluating permanent deformation, was recorded at 214 MPa, below the material's yield strength of 240 MPa. This suggests that no permanent deformation is expected under the 1300 N load.

Figure 10 shows the simulation results where some local deformation is indicated in the region of maximum stress, especially near the lattice structures. These regions with stress concentrations warrant further investigation to optimize performance and enhance the structural integrity in these localized areas.

Lattices are commonly used in AM for their ability to reduce weight while maintaining strength. However, lattice design can be complex as cell geometry must be carefully chosen to ensure structural performance and manufacturability. In this study, a hive structure lattice was selected, which achieved a nearly 50% weight reduction, resulting in a final component mass of 458 g. This design provides the required mechanical integrity while ensuring manufacturability within the LPBF process.

3.3. Roughness analysis

Despite advancements in process optimization, surface roughness in parts produced by LPBF remains highly variable. Li *et al.*[42] highlighted that laser energy density and part orientation significantly influence surface roughness. This characteristic is critical, as surface roughness directly affects the component's interaction with its environment, performance in service, and manufacturing costs.

Given the anisotropic properties of AM components, a comparative study assessed the roughness of two surfaces on the opposite sides of a complementary part. This analysis examined the W-profile in both transversal and longitudinal directions, and the same was true for the component. The study adhered to the ISO 4287[43] and ISO 25178[44] Standards. It is essential to note that only one profile was evaluated per direction, and therefore, the reported values may only partially represent the surface quality across the entire part.

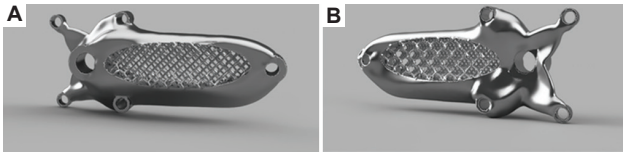

Figure 9. Illustration of the final component obtained: (A) front view, (B) back view

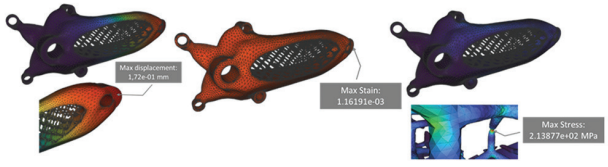

Figure 10. Results of the static test held in nTopology (1300 N)

The arithmetical mean roughness (Ra) and mean roughness depth (Rz) are widely used parameters to characterize surface roughness; however, more parameters are needed to provide more insight into surface features. Ra gives a mean value unaffected by surface variation and does not account for the shape of the surface; profiles with different geometries may share the same Ra. Similarly, Rz does not fully capture surface fluctuation details. In this study, the transversal direction exhibited a Ra of 6.71 µm, whereas the longitudinal direction had a Ra of 5.47 µm (Figure 11). The corresponding Rz values were 22.4 µm and 19.5 µm, respectively. The maximum peak height (Rp) in the transversal direction was 9.88 µm; in the longitudinal direction, it was 7.73 µm. The deepest valley (Rv) reached 12.6 µm and 11.8 µm in the transversal and longitudinal directions, respectively. The total roughness (Rt) was 33.3 µm in the transversal direction and 54.6 µm in the longitudinal direction, the latter exhibiting higher roughness due to its alignment with the build direction.

On the opposite side of the part (Figure 12), lower roughness values were observed, with a Ra of 3.56 µm in the transversal direction and 3.77 µm longitudinally. The Rz values were 12.8 µm and 14.7 µm, respectively. The maximum peak heights (Rp) were 6.07 µm in the transversal profile and 6.55 µm in the longitudinal one. The deepest valleys (Rv) were 6.75 µm and 8.10 µm, respectively. For the total roughness (Rt), the values were 31.1 µm in the transversal direction and 23.1 µm longitudinally, with the higher roughness remaining in the longitudinal direction.

It was found that overall roughness values were higher on the first face. However, these various are very common in this technology since the roughness will vary with a lot of factors, namely the position of the part relating to the argon flow, part orientation (down skins vs. up skins), and support location. Furthermore, the Roughness Directional Coefficients (Rdc) was higher on the first face, with values of 15.3 µm in the transversal and 10.9 µm in the longitudinal direction, compared to 6.93 µm and 6.54 µm on the second face. These differences in section height may have contributed to the disparity in roughness measurements.

Tribological parameters, such as skewness (Rsk) and kurtosis (Rku), provide additional insights into surface

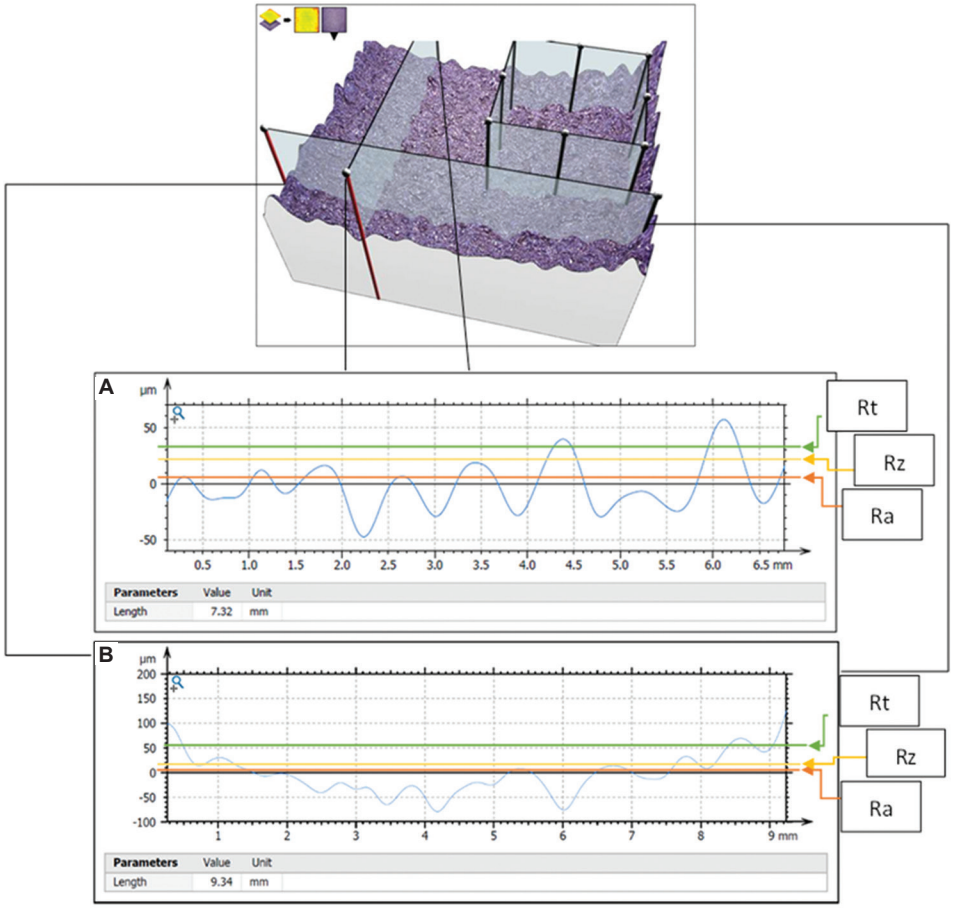

Figure 11. Cube with a prismatic shape face 1 W-profile: (A) transversal, (b) longitudinal

shape and height distribution. For the first face, the Rsk and Rku values were −0.29 and 1.96, respectively, in the transversal direction and −0.0702 and 1.91 in the longitudinal direction. For the second face, the values were −0.06 and 2.10 in the transversal direction and −0.0703 and 2.56 in the longitudinal direction. Negative Rsk values indicate surfaces with predominantly valleys, typical of sliding surfaces, whereas Rku values suggest compact surface textures without significant peaks. This is consistent with the post-treatment micro sandblasting process, which removes excess material and creates a visibly rough surface.

For the printed component (Figure 13), the mean roughness (Ra) values were 4.55 µm and 4.13 µm for the transversal and longitudinal directions, respectively. The maximum peak heights (Rp) were 5.36 µm and 5.05 µm, whereas the deepest valleys (Rv) were 8.02 µm and 8.57 µm. The total roughness (Rt) was 26.5 µm in the transversal direction and 39.5 µm in the longitudinal direction. The deeper valley in the longitudinal profile suggests inconsistent application of sandblasting post-treatment in that area.

Table 2. Comparison of the tribological values, Rsk and Rku, between the three parts

Sample	Rsk	Rku
Cube with a prismatic shape face 1		
Transversal	−0.29	1.96
Longitudinal	−0.0702	1.91
Cube with a prismatic shape face 2		
Transversal	−0.06	2.10
Longitudinal	−0.0703	2.56
Produced Component		
Transversal	0.208	2.17
Longitudinal	−0.0732	2.48

Abbreviations: Rku: kurtosis; Rsk: skewness.

Tribological values, Rsk and Rku, were used to compare the roughness of the three parts evaluated (Table 2). The roughness values for the cube with a prismatic shape face 2 were very similar to those of the printed component, which is expected since the parts were produced simultaneously

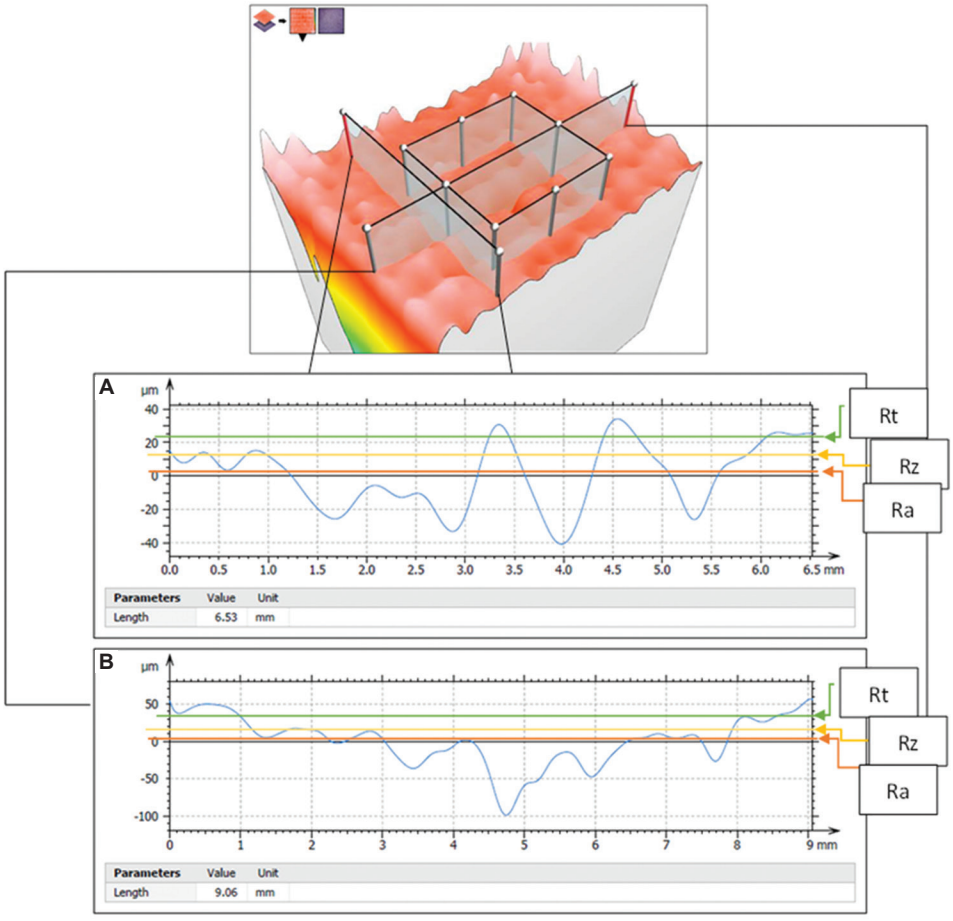

Figure 12. Cube with a prismatic shape face 2 W-profile: (A) transversal, (B) longitudinal

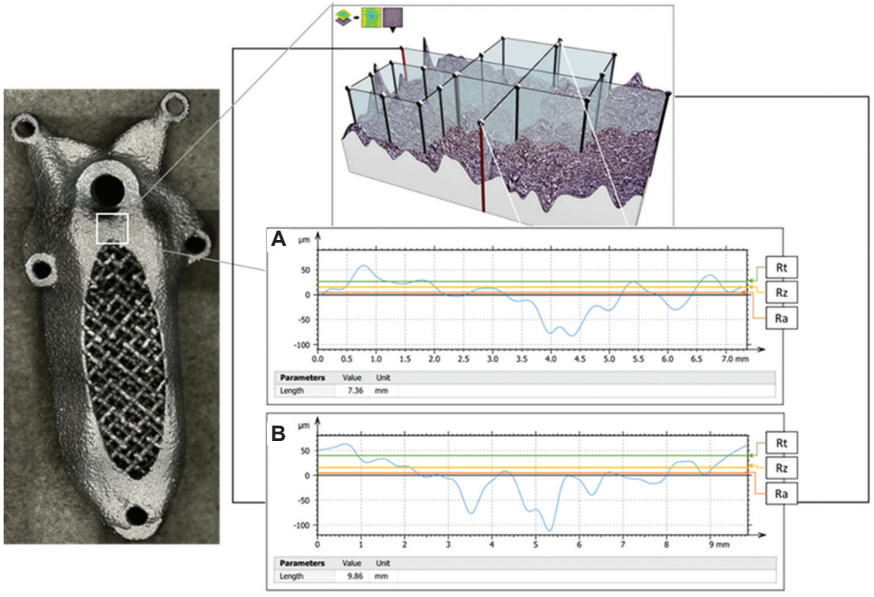

Figure 13. Printed component W-profile: (A) transversal, (B) longitudinal

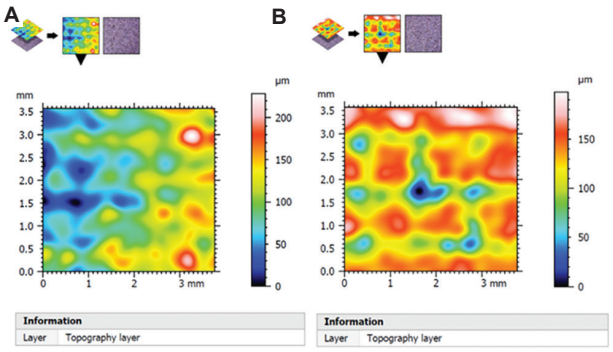

Figure 14. 3D surface texture after micro sandblasting of Alsi10Mg part: (A) transversal, (B) longitudinal

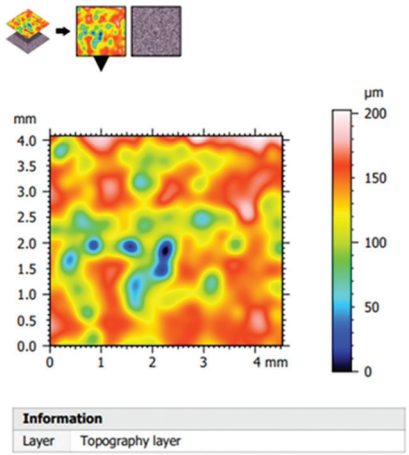

Figure 15. The 3D surface texture of the printed component after micro sandblasting Alsi10Mg part

and with the same laser parameters. The largest difference in Rsk occurs in the printed component's transversal direction. The positive Rsk in this section indicates a surface with predominantly peaks and asperities characteristic of a downskin surface, differing from the valley-dominated surfaces of the other parts (upskin surface). The down surface cloud's quality is only improved with more aggressive post-processing, such as a cycle on the vibratory tumbler.

Additional topological analysis using a 3D optical profilometer (Figure 14A and B for transversal and longitudinal, respectively) provided a more comprehensive representation of surface roughness than the 2D study. Here, roughness was expressed using areal parameters rather than directional profile measurements, with the arithmetical mean height (Sa) and maximum height (Sz) used instead of the profile-based parameters Ra and Rz. The Sa values were 30.1 µm and 25.2 µm for surfaces 1 and 2, respectively, and Sz values were 229 µm and 198 µm, respectively. The 15% reduction in roughness between the two surfaces is attributed to the micro sandblasting treatment and the natural fluctuations in the deposition process. Face 2 exhibited greater homogeneity than face 1, though neither showed symmetrical height distribution around the mean plane. Face 1 had a skewed height distribution (Ssk) below the mean plane with a value of 0.161, while face 2 had an Ssk of −0.604, indicating remaining surface peaks on face 2. This observation is consistent with the 2D data, where face 2 showed higher peak values (Sp) of 133 µm compared to 72.3 µm for face 1, while the deepest valleys (Sv) were 95.5 µm and 126 µm, respectively.

For the printed component (Figure 15), the arithmetical mean height (Sa) was 23.4 µm, while the maximum height (Sz) was 203 µm. The height distribution skewness (Ssk) was −0.812 – a higher value than that found in the cube – indicating that the printed component had greater valleys than its average height. As expected, the printed component displayed higher roughness than the cube, which is more complex geometry can explain.

Khan *et al.*[45] noted that roughness in LPBF parts is highly dependent on geometry, build position, and support volume. Horizontal surfaces typically have smoother finishes than inclined or vertical surfaces, which are more affected by the staircase effect. Larger volumes of support structures help reduce surface roughness by improving heat dissipation and reducing energy accumulation in processed layers. However, areas where the support structures are connected to the part often show localized roughness. Post-processing methods, such as sandblasting, significantly impact roughness on the surface. Mehta *et al.*[46] reported a reduced Sa of up to 43.2% after sandblasting. Parameters such as laser power and energy density can be adjusted to improve surface roughness. Maamoun *et al.*[47] achieved roughness as low as 4.5 µm by increasing energy density to 65 J/mm^3, though laser scanning speed must be carefully controlled due to its inverse relationship with roughness. Alternatively, surface treatments such as polishing shot blasting, and shot peening can further reduce roughness, with the latter reducing Sa by up to 79%.[48] However, these processes also increase production time and costs. Finally, Chu *et al.*[49] observed that satellite particles in the LPBF microstructure lead to defects such as lack of fusion, contributing to surface roughness. Visual analysis using ImageJ software and comparison to Chu *et al.*'s study suggests that the metallic powders supplied by Hypermetal had sufficient flowability and sphericity to produce a uniform topographic profile. The powder's narrow size distribution (d10, d50, and d90) did not appear to hinder the compaction process, though further analysis using laser diffraction could provide additional insights

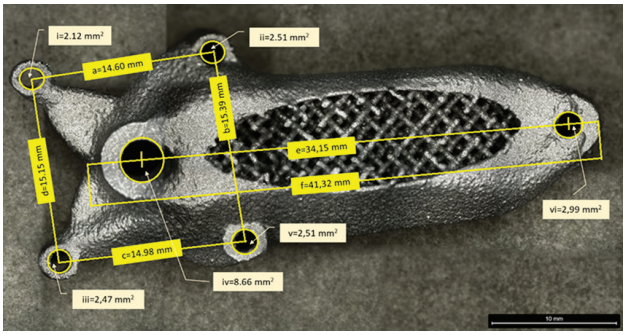

Figure 16. Features are measured directly in the component with the Leica® DVM6 and the analysis software LAX. Scale bar: 10 mm

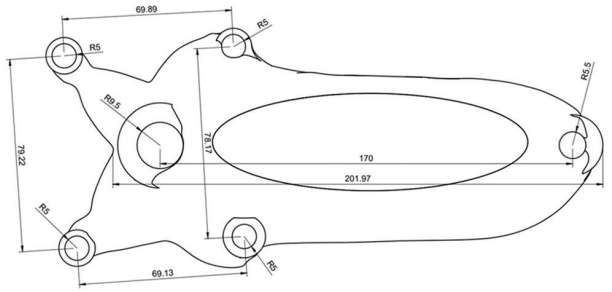

Figure 17. Technical drawing generated from the computer-aided design model and measurements of the interest features measured

into flowability and agglomeration. This would help address potential systematic errors in image processing and ensure accurate particle size measurements.

3.4. Dimensional analysis

Dimensional analysis compared measurements taken directly from the printed component using a Leica® DVM6 microscope with the dimensions specified in the original CAD model.

Figure 16 presents the raw measurement data from the Leica device, whereas Figure 17 shows the corresponding technical drawing. Since the component was produced at one-fifth of its original design size, all values in the technical drawing were divided by five to facilitate an accurate comparison. It is important to note that this scaling introduces an additional source of error that must be considered in the analysis.

For the linear dimensions (a to f), the mean difference between the printed component and the CAD model was 0.66 ± 0.39 mm, with a maximum deviation of 1.15 mm observed in dimension c. This represents a mean contraction/expansion of 3.34 ± 2.82%. The greatest contraction was recorded for measurement d (4.38%), while the largest expansion was observed in dimension c (8.35%).

The results indicate that the dimensional accuracy of the printed component does not meet the requirements for integration into a functional bicycle component, where high precision is essential. The most problematic deviations were observed in the holes intended for screw threads, where significant reductions in available space could compromise the component's functionality. Achieving greater dimensional accuracy is paramount, particularly for applications where precision is critical.

Dimensional accuracy in LPBF can be influenced by several factors, including powder quality, laser energy density, scanning speed, layer thickness, and the part's positioning relative to the assisted gas nozzle. In addition, material shrinkage during solidification plays a critical role, with the thermal expansion coefficient for this material being 2.1×10^{-5} mm/°C.[17] Although the laser path is typically programmed to account for this shrinkage, variations in powder quality, which were not accounted for in this study, may have contributed to the observed deviations. Other sources of error in this analysis stem from the manual nature of the measurements. Geometric figures were drawn manually on images captured with the optical microscope, as seen in Figure 17.

Furthermore, the conversion of dimensional values before comparison introduces additional uncertainty. These factors, combined with the laser spot diameter of 70 µm used for this build, suggest that the reduced size of the component led to lower dimensional accuracy, as finer details could not be captured with precision. Despite these challenges, the overall dimensional accuracy of the component can be considered acceptable, given the reduction in scale. However, the component should be fully scaled and analyzed using a Coordinate-Measuring Machine (CMM) to ensure the highest accuracy. A CMM would enable reverse engineering of the printed part, generating a new CAD model based on the actual measurements of the printed component. This model could then be compared directly with the original design, allowing for a more thorough evaluation of dimensional accuracy.

3.5. Hardness and material properties

In this study, the higher hardness of the AlSi10Mg component compared to similar studies in the literature can be attributed to differences in microstructure, particularly the grain size or the number of different phases (*e.g.*, precipitates) formed during the AM process. While the parts in this study and those in the literature exhibit similar relative densities, and both sets of parts are defect-free with no porosity, the microstructural features could contribute significantly to the observed variations in hardness.

Although the parts in this study and the literature used optimized process parameters to achieve highly dense, defect-free parts, it is possible that differences in the microstructure, such as finer or coarser grains or the presence of different phases, could lead to changes in hardness. These factors influence the mechanical properties of materials, including hardness, and may explain the higher hardness in our study compared to literature values.[50,51]

Thus, the higher hardness observed in this study is not solely due to differences in powder characteristics or densification but is more likely attributable to microstructural differences, including grain size and precipitates or other phases. Further studies focusing on the microstructure characterization in both this study and the literature would provide a more comprehensive understanding of how these factors contribute to variations in hardness and other mechanical properties.

4. Conclusions

This study explored a bicycle crank's TO and AM in AlSi10Mg using LPBF. The research successfully developed a lightweight and structurally optimized component by integrating advanced design strategies such as lattice structures. Rigorous testing and analysis validated the prototype's compliance with standards, manufacturability, and mechanical performance. The findings underscore the potential of TO and LPBF for creating high-performance, lightweight components while identifying areas for further improvement. Key conclusions drawn from this study are as follows:

- Component achievement:
  - Successfully designed and manufactured a topology-optimized bicycle crank in AlSi10Mg using LPBF
  - The single-part component complies with ISO 14781 and was validated through static testing
  - A lightweight design of 458 g was achieved by incorporating lattice structures into the topology-optimized component
  - Despite the production process's complexity, careful lattice cell selection ensured the successful fabrication of a functional prototype.
- Validation and testing:
  - Microstructure analysis:
    - Revealed elongated melt pools aligned with the scan direction, consistent with LPBF technology
    - Confirmed the absence of excessive porosity, ensuring manufacturing integrity.
- Surface roughness analysis:
  - Highlighted the impact of process variables, including part orientation, argon flow, supports, and post-processing
  - Identified limitations in surface quality inherent to LPBF technology, suggesting potential improvements through optimized process parameters or advanced post-processing methods such as vibratory tumbling or electrochemical polishing
  - Findings emphasize the importance of refining process parameters and post-processing techniques to achieve a smoother surface finish, which is critical for improving esthetic quality and tribological performance.
- Tribological investigations:
  - Surface roughness is critical in tribological performance, influencing friction and wear behavior
  - The tribological behavior of the component showed that surface roughness values directly correlate with friction and wear performance. Further optimization of the surface texture through post-processing may enhance the component's durability and functionality in real-world applications.
- Dimensional analysis:
  - Demonstrated variability in dimensional accuracy, with deviations of 0.66 ± 0.39 mm for lengths and 0.12 ± 0.05 mm for circle radii
  - Suggested improvements through additional supports, changes in part orientation, or adjustments to the geometry for enhanced manufacturability.
- Material and powder characteristics:
  - The narrow particle size distribution of AlSi10Mg powders facilitated consistent production results despite a 40% satellite particle presence.
- Considerations for future studies:
  - Conduct more detailed roughness studies, focusing on stair-stepping effects
  - Define dimensional tolerances for prototypes to enhance validation accuracy
  - Investigate the effects of particle size distribution and satellite particle percentages on the component's mechanical and surface properties
  - Explore scalability and economic feasibility for potential industrial applications
  - Examine the tribological performance of the component in greater detail, including wear resistance and friction in operational conditions
  - Further, optimize post-processing methods to enhance surface quality and tribological performance.

This research highlights the transformative potential of TO and LPBF in producing lightweight, high-performance components. It also identifies areas that need improvement to encourage broader industrial adoption. Future studies should concentrate on detailed microstructural analysis and the influence of process parameters on mechanical properties, particularly hardness. In addition, examining factors such as residual stresses, thermal gradients, and powder characteristics – such as particle size distribution and packing density – will offer valuable insights into optimizing component performance and consistency. These efforts will help bridge the gaps in understanding and enable more precise control over the manufacturing process for industrial applications.

Acknowledgments

This work results from Agenda "Hi-Rev – Recuperação do Setor de Componentes Automóveis", nr. C644864375-00000002, investment project nr. 64, financed by the Recovery and Resilience Plan (PRR) and by the European Union-NextGeneration EU.

Funding

This research received no external funding.

Conflicts of interest

The authors declare no conflicts of interest.

Author contributions

Conceptualization: Jose Manuel Costa, Manuel Fernando Vieira, Elsa Wellenkamp Sequeiros

Formal analysis: Jose Manuel Costa, Elsa Wellenkamp Sequeiros, Manuel Fernando Vieira

Investigation: Adriana Pinho Fernandes, Elsa Costa Oliveira, Mariana Cerqueira Maia, Jose Manuel Costa, Elsa Wellenkamp Sequeiros;

Methodology: Jose Manuel Costa, Elsa Wellenkamp Sequeiros;

Project administration: Jose Manuel Costa, Elsa Wellenkamp Sequeiros;

Supervision: Jose Manuel Costa, Manuel Fernando Vieira, Elsa Wellenkamp Sequeiros;

Validation: Jose Manuel Costa, Elsa Wellenkamp Sequeiros;

Visualization: Adriana Pinho Fernandes, Elsa Costa Oliveira, Mariana Cerqueira Maia, Jose Manuel Costa, Elsa Wellenkamp Sequeiros

Writing–original draft: Adriana Pinho Fernandes, Elsa Costa Oliveira, Mariana Cerqueira Maia, Jose Manuel Costa, Elsa Wellenkamp Sequeiros

Writing–review and editing: Jose Manuel Costa, Elsa Wellenkamp Sequeiros

All authors have read and agreed to the published version of the manuscript.

Ethics approval and consent to participate

Not applicable.

Consent for publication

Not applicable.

Availability of data

Not applicable.

References

1. Costa JM, Sequeiros EW, Santos RF, Vieira MF. Benchmarking L-PBF systems for die production: Powder, dimensional, surface, microstructural and mechanical characterisation. *Metals Basel.* 2024;14:520

   doi: 10.3390/met14050520

2. ISO/ASTM. *ISO/ASTM 52900: 2021-Additive Manufacturing-General Principles-Fundamentals and Vocabulary*. London: ISO; 2021. p. 28.

3. Pei E. *Springer Handbook of Additive Manufacturing*. Berlin: Springer; 2023.

4. Bar-Cohen Y. *Advances in Manufacturing and Processing of Materials and Structures*. United States: CRC Press; 2018.

5. Ford S, Despeisse M. Additive manufacturing and sustainability: An exploratory study of the advantages and challenges. *J Clean Prod.* 2016;137:1573-1587.

   doi: 10.1016/j.jclepro.2016.04.150

6. Costa JM, Sequeiros EW, Vieira MF. Fused filament fabrication for metallic materials: A brief review. *Materials.* 2023;16:7505.

   doi: 10.3390/ma16247505

7. Zutin GC, Pulquerio EC, Pasotti AV, Barbosa GF, Shiki SB. Application of robotic manipulator technology and its relation to additive manufacturing process-a review. *Int J Adv Manuf Technol.* 2024;133:257-271.

   doi: 10.1007/s00170-024-13710-9

8. Prakash KS, Nancharaih T, Rao VVS. Additive manufacturing techniques in manufacturing -an overview. *Mater Today Proc.* 2018;5:3873-3882.

   doi: 10.1016/j.matpr.2017.11.642

9. Zhou L, Miller J, Vezza J, *et al*. Additive manufacturing: A comprehensive review. *Sensors.* 2024;24:2668.

   doi: 10.3390/s24092668

10. Gibson I, Rosen DW, Stucker B. *Additive Manufacturing Technologies: Rapid Prototyping to Direct Digital Manufacturing*. New York: Springer US; 2010.

11. Costa J, Sequeiros E, Vieira MT, Vieira M. Additive manufacturing: Material extrusion of metallic parts. *U Porto J Eng.* 2021;7:53-69.

doi: 10.24840/2183-6493_007.003_0005

12. Gebhardt A, Kessler J, Thurn L. 5 Perspectives and Strategies of Additive Manufacturing. In: *3D Printing.* 2nd ed. Germany: Hanser; 2019. p. 137-165.

13. Gibson I, Rosen D, Stucker B, Khorasani M. *Binder Jetting.* Berlin: Springer International Publishing; 2021. p. 237-252.

14. Egan PF. Design for additive manufacturing: Recent innovations and future directions. *Designs.* 2023;7:83.

doi: 10.3390/designs7040083

15. Chen H, Wei Q, Wen S, Li Z, Shi Y. Flow behavior of powder particles in layering process of selective laser melting: Numerical modeling and experimental verification based on discrete element method. *Int J Mach Tool Manuf.* 2017;123:146-159.

16. Sun X, Chen M, Liu T, *et al*. Characterization, preparation, and reuse of metallic powders for laser powder bed fusion: A review. *Int J Extreme Manuf.* 2024;6:012003.

doi: 10.1088/2631-7990/acfbc3

17. Veetil JK, Khorasani M, Ghasemi A, *et al*. Build position-based dimensional deviations of laser powder-bed fusion of stainless steel 316L. *Precis Eng.* 2021;67:58-68.

doi: 10.1016/j.precisioneng.2020.09.024

18. Sehhat MH, Mahdianikhotbesara A. Powder spreading in laser-powder bed fusion process. *Granular Matter.* 2021;23:89.

doi: 10.1007/s10035-021-01162-x

19. Parteli EJR, Poschel T. Particle-based simulation of powder application in additive manufacturing. *Powder Technol.* 2016;288:96-102.

doi: 10.1016/j.powtec.2015.10.035

20. Haferkamp L, Haudenschild L, Spierings A, *et al*. The influence of particle shape, powder flowability, and powder layer density on part density in laser powder bed fusion. *Metals-Basel.* 2021;11:418.

doi: 10.3390/met11030418

21. Mostafaei A, Ghiaasiaan R, Ho IT, *et al*. Additive manufacturing of nickel-based superalloys: A state-of-the-art review on process-structure-defect-property relationship. *Prog Mater Sci.* 2023;136:101108.

doi: 10.1016/j.pmatsci.2023.101108

22. Costa JM, Vieira MF. Teaching design for AM to science materials engineering graduate students: Hand-on approach. *Modern Concepts Mater Sci.* 2024;6.

doi: 10.33552/MCMS.2024.06.000640

23. Costa JM, Sequeiros EW, Figueiredo D, Reis AR, Vieira MF. *Optimizing Metal AM Potential through DfAM: Design, Performance, and Industrial Impact*. London: IntechOpen; 2024.

24. Oliveira C, Maia M, Costa J. Production of an office stapler by material extrusion process, using DfAM as optimization strategy. *U Porto J Eng.* 2023;9:28-41.

doi: 10.24840/2183-6493_009-001_001635

25. Brackett D, Ashcroft I, Hague R. Topology optimization for additive manufacturing. In: *Proceedings of the 22nd Annual International Solid Freeform Fabrication Symposium-An Additive Manufacturing Conference*, SFF 2011, Austin, TX; 2011. p. 348-362.

26. Plocher J, Panesar A. Review on design and structural optimisation in additive manufacturing: Towards next-generation lightweight structures. *Mater Design.* 2019;183:108164.

doi: 10.1016/j.matdes.2019.108164

27. Ibhadode O, Zhang Z, Sixt J, *et al*. Topology optimization for metal additive manufacturing: Current trends, challenges, and future outlook. *Virtual Phys Prototy.* 2023;18:2181192.

doi: 10.1080/17452759.2023.2181192

28. Diegel O, Nordin A, Motte D. *A Practical Guide to Design for Additive Manufacturing*. Berlin: Springer; 2019.

29. ASM International. *Aluminum Science and Technology.* Vol. 2A. Netherlands: ASM International; 2018.

doi: 10.31399/asm.hb.v02a.9781627082075

30. Su J, Ng WL, An J, Yeong WY, Chua CK, Sing SL. Achieving sustainability by additive manufacturing: A state-of-the-art review and perspectives. *Virtual Phys Prototyp.* 2024;19:e2438899.

doi: 10.1080/17452759.2024.2438899

31. Sbrugnera Sotomayor NA, Caiazzo F, Alfieri V. Enhancing design for additive manufacturing workflow: Optimization, design and simulation tools. *Appl Sci.* 2021;11:6628.

doi: 10.3390/app11146628

32. Mata M, Pinto M, Costa J. Topological optimization of a metal extruded doorhandle using ntopology. *U Porto J Eng.* 2023;9:42-54.

doi: 10.24840/2183-6493_009-001_001620

33. Rometsch PA, Zhu Y, Wu X, Huang A. Review of high-strength aluminium alloys for additive manufacturing by laser powder bed fusion. *Mater Design.* 2022;219:110779.

doi: 10.1016/j.matdes.2022.110779

34. Tofail SAM, Koumoulos EP, Bandyopadhyay A, Bose S, O'Donoghue L, Charitidis C. Additive manufacturing: Scientific and technological challenges, market uptake and opportunities. *Mater Today.* 2018;21:22-37.

doi: 10.1016/j.mattod.2017.07.001

35. Shimano. *Shimano SLX M7000 Hollowtech II Crank*.

Available from: https://bike.shimano.com/technologies/details/hollowtech-2.html [Last accessed on 2024 Jul 10].

36. ISO. *ISO/IEC/IEEE 14764:2022-Software Engineering-Software Life Cycle Processes-Maintenance*. Switzerland: ISO; 2022. p. 36.
37. Sandvik. *Osprey® AlSi10Mg Powder for Additive Manufacturing - DATASHEET*. Available from: https://www.metalpowder.sandvik/en/syssiteassets/metal-powder/datasheets/osprey-alsi10mg-and-alsi7mg.pdf [Last accessed on 2024 Oct 19].
38. Li P, Kim Y, Bobel AC, *et al*. Microstructural origin of the anisotropic flow stress of laser powder bed fused AlSi10Mg. *Acta Mater.* 2021;220:117346.

    doi: 10.1016/j.actamat.2021.117346
39. Zhou L, Mehta A, Schulz E, McWilliams B, Cho K, Sohn Y. Microstructure, precipitates and hardness of selectively laser melted AlSi10Mg alloy before and after heat treatment. *Mater Charact.* 2018;143:5-17.

    doi: 10.1016/j.matchar.2018.04.022
40. Aboulkhair NT, Simonelli M, Parry L, Ashcroft I, Tuck C, Hague R. 3D printing of aluminium alloys: Additive manufacturing of aluminium alloys using selective laser melting. *Progress Mater Sci.* 2019;106:100578.

    doi: 10.1016/j.pmatsci.2019.100578
41. Mower TM, Long MJ. Mechanical behavior of additive manufactured, powder-bed laser-fused materials. *Mater Sci Eng A*. 2016;651:198-213.

    doi: 10.1016/j.msea.2015.10.068
42. Li BQ, Li Z, Bai P, Liu B, Kuai Z. Research on surface roughness of AlSi10Mg parts fabricated by laser powder bed fusion. *Metals Basel.* 2018;8:524.

    doi: 10.3390/met8070524
43. ISO_4287. *Geometrical Product Specifications (GPS)-Surface Texture: Profile Method-Terms, Definitions and Surface Texture Parameters*. Switzerland: ISO; 1997.
44. ISO/ASTM. *ISO 25178-600:2019-Geometrical Product Specifications (GPS)-Surface Texture: Areal-Part 600: Metrological Characteristics for Areal Topography Measuring Methods*. Switzerland: ISO; 2019. p. 21.
45. Khan HM, Karabulut Y, Kitay O, Kaynak Y, Jawahir IS. Influence of the post-processing operations on surface integrity of metal components produced by laser powder bed fusion additive manufacturing: A review. *Machining Sci Technol.* 2021;25:118-176.

    doi: 10.1080/10910344.2020.1855649
46. Mehta B, Hryha E, Nyborg L, Tholence F, Johansson E. Effect of surface sandblasting and turning on compressive strength of thin 316L stainless steel shells produced by laser powder bed fusion. *Metals Basel.* 2021;11:1070.

    doi: 10.3390/met11071070
47. Maamoun AH, Xue YF, Elbestawi MA, Veldhuis SC. Effect of selective laser melting process parameters on the quality of al alloy parts: Powder characterization, density, surface roughness, and dimensional accuracy. *Materials.* 2018;11:2343.

    doi: 10.3390/ma11122343
48. Sagbas B. Post-processing effects on surface properties of direct metal laser sintered AlSi10Mg parts. *Metals Mater Int.* 2020;26:143-153.

    doi: 10.1007/s12540-019-00375-3
49. Chu F, Zhang K, Shen H, *et al*. Influence of satellite and agglomeration of powder on the processability of AlSi10Mg powder in Laser Powder Bed Fusion. *J Mater Res Technol.* 2021;11:2059-2073.

    doi: 10.1016/j.jmrt.2021.02.015
50. Al Njjar A, Mazloum K, Sata A. Optimization of powder metallurgy parameters for improving the major properties of AA7075/SiC composites for aerospace applications. *J Mater Eng Perform.* 2024.

    doi: 10.1007/s11665-024-09998-z
51. Zhang P, Li X, Dong S, *et al*. Superhigh yield ratio and considerable plasticity in powder metallurgy Al-Zn-Mg-Cu alloy prepared with elemental powder. *JOM.* 2024;77:1241-1251.

    doi: 10.1007/s11837-024-07018-y